

Supporting Information for

# Surface Structure of Aerobically Oxidized Diamond Nanocrystals

*Abraham Wolcott<sup>†,\*</sup>,<sup>□,δ,Δ</sup>, Theanne Schiros<sup>Ψ</sup>, Matthew E. Trusheim<sup>\*,□,δ</sup>, Edward H. Chen<sup>\*,□,δ</sup>,  
Dennis Nordlund<sup>Σ</sup>, Rosa E. Diaz<sup>Ω</sup>, Ophir Gaathon<sup>\*,□,Δ</sup>, Dirk Englund<sup>\*,□,δ</sup> and Jonathan S.  
Owen<sup>†,\*</sup>*

<sup>†</sup>Department of Chemistry, Columbia University, New York, NY 10027

<sup>\*</sup>Department of Electrical Engineering, Columbia University, New York, NY 10027

<sup>□</sup>Department of Applied Mathematics and Applied Physics, Columbia University, New York, NY 10027

<sup>δ</sup>Department of Electrical Engineering and Computer Science, Massachusetts Institute of Technology, Cambridge, MA 02139

<sup>Ψ</sup>Energy Frontier Research Center, Columbia University, New York, New York 10027

<sup>Σ</sup>Stanford Synchrotron Radiation Light Source, SLAC National Accelerator Laboratory, Menlo Park, CA 94025

<sup>Ω</sup>Center for Functional Nanomaterials, Brookhaven National Laboratory, Upton, NY 11973

<sup>Δ</sup>Diamond Nanotechnologies Inc., Boston, MA 02134

Corresponding authors: \*awolcott@mit.edu, \*jso2115@columbia.edu

**Measuring  $sp^2$  :  $sp^3$  ratio.**  $sp^2:sp^3$  ratios were determined through the integration of the  $\pi^*_{C=C}$  resonance from 284.0 - 286.0 eV and the  $\sigma^*$  resonance from 293.0 - 302.0 eV with a cleaved HOPG sample as the 100%  $sp^2$  control.<sup>1-3</sup> All other HPHT ND related samples were analyzed in the same manner as the HOPG control sample, and the  $sp^3$  content was calculated through the ratios of  $\pi^*_{C=C}$  and  $\sigma^*$  resonances as described by:<sup>1-3</sup>

$$\% sp^2_{HPHT\ NDs} \approx \frac{(\pi^*/\sigma^*)_{HPHT\ ND}}{(\pi^*/\sigma^*)_{HOPG}} \quad (1)$$

$$\% sp^3_{HPHT\ NDs} = 100\% - \% sp^2_{HPHT\ NDs} \quad (2)$$

$sp^2$  :  $sp^3$  ratios were also determined by a point intensity method wherein, absolute intensity of the  $\pi^*_{C=C}$  resonance at 285.0 eV and the core-exciton intensity at 291.5 eV for HOPG was used as the 100%  $sp^2$  control sample similar to the integration method. The same point intensity value was then applied for the HPHT ND samples at 285.0 eV for the  $\pi^*_{C=C}$  resonance and the core-exciton at 289.0 eV, and their ratio applied as

$$\% sp^2_{HPHT\ NDs} \approx \frac{(\frac{\pi^* Peak Int}{\sigma^* Peak Int})_{HPHT\ ND}}{(\frac{\pi^* Peak Int}{\sigma^* Peak Int})_{HOPG}} \quad (3)$$

The integration and peak intensity values were then averaged and their standard deviation calculated and plotted. Integration values were higher in  $sp^2$  content then the peak intensity method, but the trend in the data was consistent over the two analytical methods.

**Diffuse Reflectance Infrared Fourier Transform Spectroscopy (DRIFTS).** DRIFTS was performed on a Thermo-Nicolet 7800 FTIR with a Harrick Scientific Praying Mantis<sup>TM</sup> diffuse reflectance accessory, a liquid nitrogen cooled MCT detector and KBr beamsplitter. Samples were ground in a mortar and pestle in dry KBr. Measurements were performed with 128 or 256 scans at a resolution of 2  $cm^{-1}$  and background scans of near or equal signal intensity. Kubelka-Munk transformations were performed individually with linear background corrections. Linear

background were calculated based on the averaged values of percent reflectance (raw data) in the regions of 2000 - 2200  $\text{cm}^{-1}$  and 3800 - 4000  $\text{cm}^{-1}$ . This slope value was then applied to a y-intercept function ( $y=mx+b$ ) and applied to spectra for normalized reflectance units (R) and then transformed using the Kubleka-Munk equation to make the data proportional to concentration:

$$KM\ Units = \frac{(1 - R^2)}{2R}$$

Infrared values were cross referenced to *Infrared and Raman characteristic group frequencies: tables and charts* by Socrates, as well as prior references to both DND and HPHT ND studies.<sup>1,4-</sup>

7

**Photoelectron Escape Depth.** The approximate kinetic energy of a photoelectron produced by photoexcitation with 410 eV X-ray radiation is 125 eV. At 125 eV the electron mean free path of carbon K shell photoelectrons are ~0.5 nm and the normalization coefficient for photoabsorption ( $\sigma$ ) is ~0.4, according to Yeh and Lindau.<sup>8</sup> In a single crystal diamond sample ~0.5 nm is approximately 2.5 and 1.4 atomic layers on the {111} and {100}, respectively. The approximate kinetic energy of a photoelectron produced by photoexcitation with 950 eV X-ray radiation is ~665 eV. At 665 eV the electron mean free path of carbon K shell photoelectrons are ~1.0 nm and the normalization coefficient for photoabsorption ( $\sigma$ ) is ~0.05.<sup>8</sup> In a single crystal diamond sample ~1.0 nm is approximately 5 and 2.8 atomic layers on the {111} and {100}, respectively.

**Deconvolution of Photoelectron Spectra.** Peak fitting was performed with a mixed Lorentzian/Gaussian lineshape (Voigt) with initial peak positions based on bulk diamond photoelectron spectra.<sup>9-12</sup> Peak position and linewidth fitting was performed using Multi-peak Fitting 2 in Igor Pro based on least squares analysis. Typical fitting values for Lorentzian and Gaussian contributions were approximately ~15% and ~85% respectively.<sup>13</sup> Peak positions were held constant with values consistent with bulk diamond (ex. C-C at ~285.0 eV and C-O-H at 286.5 eV) while FWHM, area and Lorentzian/Gaussian contributions were floating parameters. Error in the percentage of peak contributions is estimated at 50%. A bulk diamond component at 285.3 eV with 410 eV and 950 eV photons is consistent with positive electron affinities of oxygen terminated diamond surfaces and is thought to be caused by the dipole generated by the

C-O bonds and their effect on surface potential and is in the range of previously cited  $sp^3$  diamond.<sup>7,14,15</sup> Surface sensitive XPS on the partially oxidized sample (500 °C, 2 hrs.) revealed strong photoemission from  $sp^2$  hybridized carbons at 283.9 eV; a chemical shift of -1.4 eV from bulk diamond.<sup>16</sup> This component is no longer observed after purification at 575 °C. Both 500 °C and 575 °C samples have surface species with chemical shifts of 1.0 - 1.2 eV (286.3 - 286.5 eV) and 3.7 - 4.6 eV (289.0 - 289.9 eV) that are assigned to alcohols and C=O groups.<sup>7,17</sup> The chemical shift of the minor component relative to bulk diamond is consistent with its assignment as an acid/acid anhydride functional group.

Table 1 describes the contributions to the normalized electron yield from the HPHT ND samples as a function of surface and bulk contributions. Photoemission yield was normalized to the wavelength dependent absorption coefficient as described by Leh and Lindau.<sup>8</sup> Partially oxidized samples show signals from graphitic carbons that contribute 17.4% of the total signal that decreases to 10.1 % at 950 eV. The sample oxidized at 575 °C for 2 hours showed no apparent signal from graphitic carbon at both wavelengths. The signal from bulk diamond carbon ranged from 15.0 - 54.2 % with the maximum contribution from the 575 °C sample with 950 eV light. Contributions from alcohols (C-O) were observed in the range of 38.5 - 65.6 % with the 500 °C showing the largest contributions. Photoelectrons from acid/acid anhydrides (C=O) ranged from 2.0 - 7.3 % in total electron yield, and was consistent with our DRIFTS measurements of an acid/acid anhydride poor surface.

**Table 1:** Summary of Wavelength Dependent XPS Spectra at 410 and 950 eV.

Wavelength (eV)	Oxidation Temperature °C	Graphitic Carbon %	Diamond %	C-O %	C=O %
410 <sup>a</sup>	575°C	0	42.0	52.3	5.7
410 <sup>a</sup>	500°C	17.4	15.0	65.6	2.0
950 <sup>b</sup>	575°C	0	54.2	38.5	7.3
950 <sup>b</sup>	500°C	10.1	30.6	56.8	2.5



**Figure S1.** Photographs of bulk and ball milled HPHT diamond following aerobic oxidation for 2 hours over a range of temperatures.

**Single Nitrogen Vacancy Center Microscopy.** Single NVCs were studied using with a home built oil immersion confocal microscope setup ( $NA = 1.3$ ) based on a Zeiss microscope (AxioObserver) that is diagrammed in Scheme S1 below. A confocal scanning microscopy image of aerobically oxidized NDs is shown in Figure S2 along with the fluorescence spectrum of a single NV<sup>-</sup> center that was confirmed with photon correlation spectroscopy (Figures 7B,C). The zero-phonon emission line at 637.8 nm and an optically detected ESR spectrum (Figure 7D) are characteristic of the NV<sup>-</sup> triplet ground state; no evidence for neutral NVCs was obtained. The degeneracy of the  $m_s = \pm 1$  levels was lifted by a small external magnetic field. Surface functionality is known to influence the charge state of NVCs, with C-O and C-H terminated diamond surfaces leading to positive and negative electron affinity surfaces, respectively.<sup>14,18-20</sup> Similarly, surface oxidation has been shown to affect the charge state of shallow NVCs in bulk diamond.<sup>21,22</sup> Thus, aerobic oxidation of HPHT NDs leads to native NV<sup>-</sup> centers that can be exploited for magneto sensing applications.

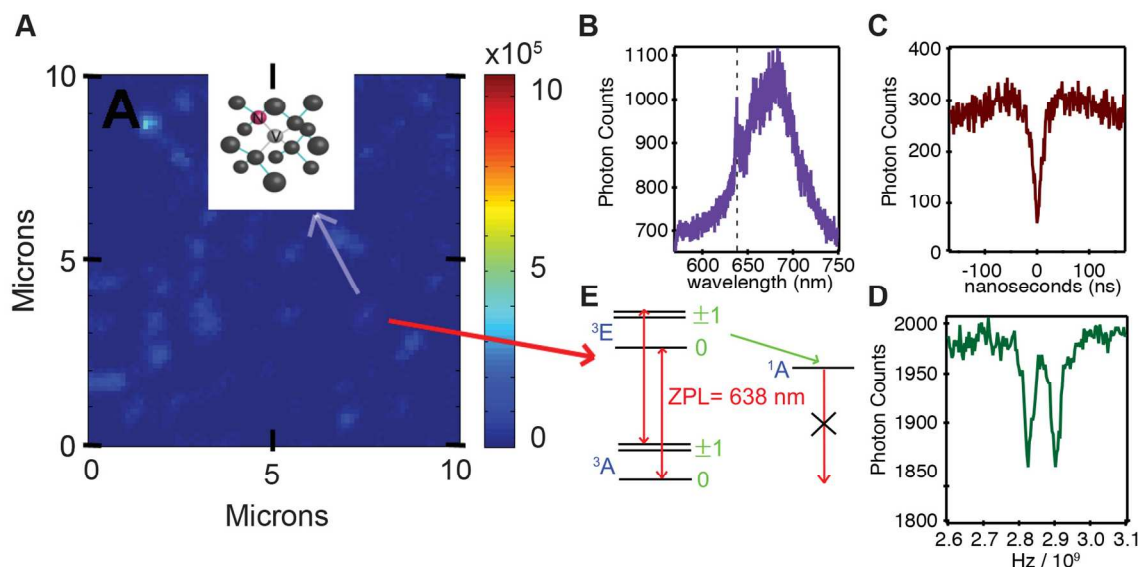
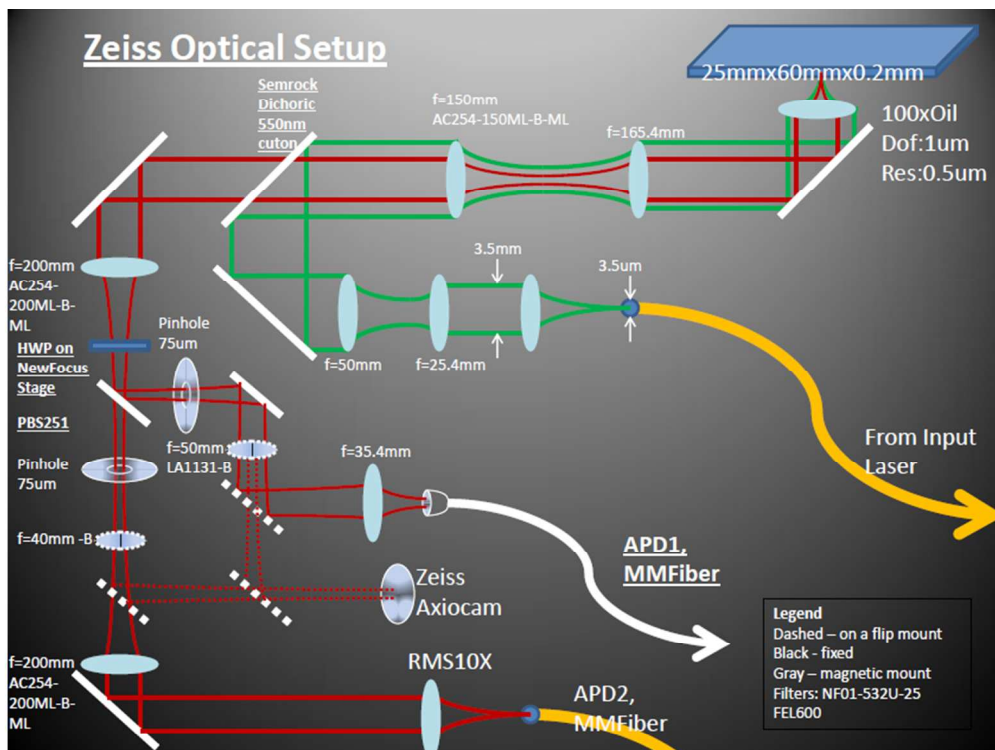


**Figure S2.** (A) A confocal scanning microscope image of fluorescent HPHT NDs after aerobic oxidation at 575°C for 2 hours ( $\lambda_{\text{excitation}} = 532$  nm). Luminescence from negatively charged nitrogen vacancy centers (A - inset) is confirmed by the fluorescence spectrum (B) of a single emitter with a zero phonon line at 638 nm. (C) Photon correlation measurements ( $g^{(2)}$ ) reveals a decrease at  $g^{(2)}(\tau)$  of more than 0.5 confirming the emission is from a single emitter. Optically

detected CW-ESR spectrum (**D**) near 2.87Ghz are those expected from the energy level splitting of a single nitrogen vacancy center within a small magnetic field (**E**).



**Scheme S1.** Oil immersion confocal scanning Zeiss microscope setup for single NVC detection is outlined above. Photoexcitation was with a 532 nm diode laser, and light collection was performed with a pair of avalanche photo diodes (APDs) and a single photon counting board. Polarization and wavelength selection was performed with  $\lambda/2$  waveplates and dichroic optics along with pinholes for reduced background photon counts.

## Transmission Electron Microscopy

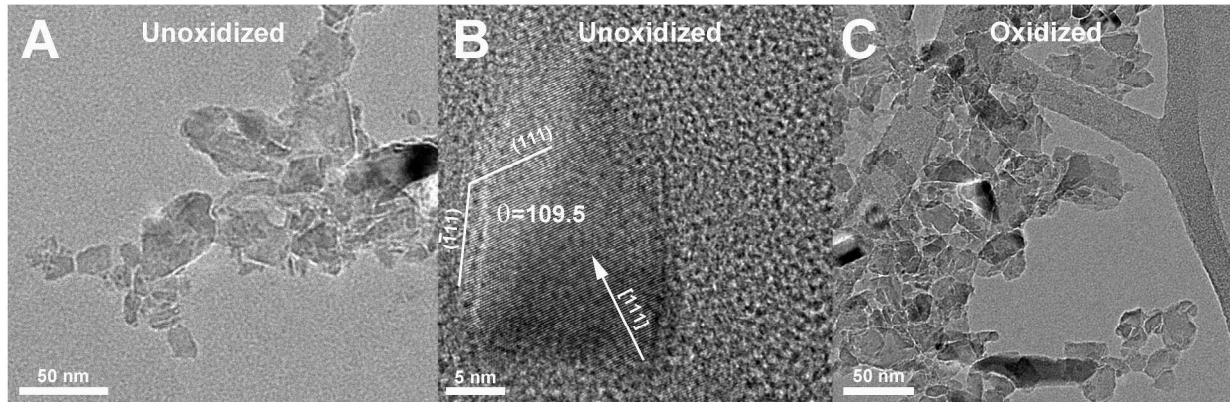


**Figure S3.** A collection of HPHT NDs with shard-like morphology imaged at 200 keV (A). HPHT ND samples were stable under high magnification for extended periods of time without degradation of their crystal structure. A 15 nm  $\times$  20 nm HPHT ND that was unoxidized shows crystal lattice facets that could be indexed to the [111] and the two white lines are a guide to the eye which represent the (111) and  $(\bar{1}11)$  planes at an angle of  $\theta = 109.5^\circ$  (B). High resolution images were more easily obtained on oxidized samples. Oxidized and unoxidized HPHT NDs at low magnification are similarly shaped and range in size from 5-40 nm.

## Nanocrystal Sizes Before and After Oxidation As Measured by Transmission Electron Microscopy

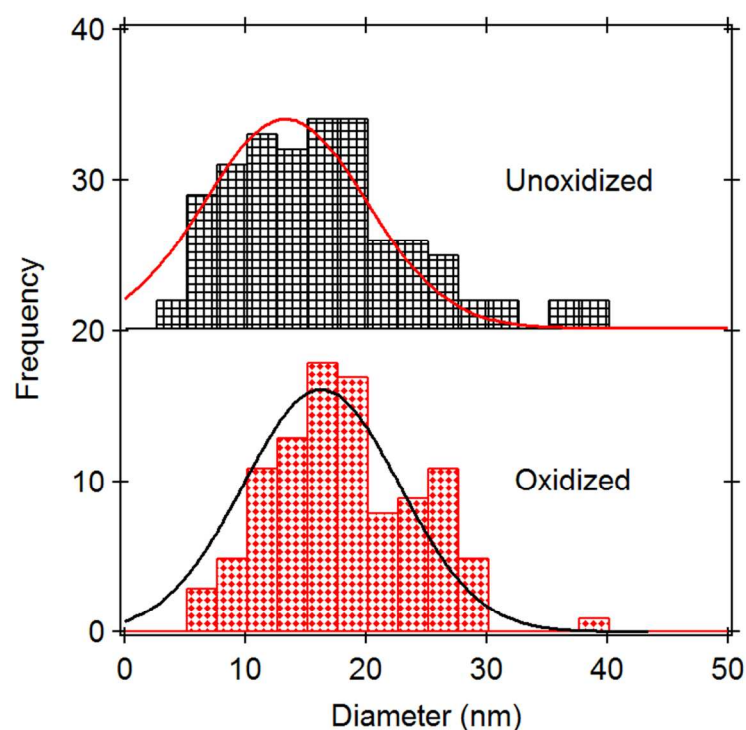


**Figure S4.** Histograms of unoxidized and oxidized (575 °C for 2 hours) HPHT NDs showing that the oxidation has a minimal impact on the size distribution. The area of the ND projection was used to calculate the diameter of a sphere with an equivalent area of projection. The anisotropy of the NDs makes this a slight over estimate of the actual size. A Gaussian fit to this histogram shows an average diameter of  $13.3 \pm 15.8$  nm for the unoxidized material. After oxidation the equivalent diameter is  $16.3 \pm 15.3$  nm. The slight increase may be caused by the greater instability of the smallest diameter NDs.



## XRD Reinforces Higher Crystalline Content and Lack of Graphite

The superior crystallographic structure of HPHT NDs in comparison to DND and lack of graphitic carbon is reinforced by powder XRD. XRD signatures of HPHT powders before and after oxidation have standard peak positions and narrower linewidths than DND and compliment the previous observations of the core-hole diamond exciton and strong  $\Gamma$  phonon mode via Raman scattering. The HPHT ND 111 diffraction peak was observed at  $2\theta=44.14$ , within error of the bulk diamond standard at  $44.1409$  (JCPDS #001-1249). In contrast, DND powder reflections for 111 were found to be  $2\theta=43.85$ , shifted due to strain and defects as discussed elsewhere.<sup>23</sup> HPHT NDs have narrower linewidths both before and after aerobic oxidation (instrumental broadening correction of  $2\theta=0.2$  applied). The Gaussian linewidths of HPHT NDs decrease from  $\Delta 2\theta=0.509 \rightarrow 0.409$  (111) before and after oxidation and have calculated grain sizes of 28.9 nm and 42.8 nm. TEM analysis and DLS (mean particle size of  $\sim 30$  nm) does not show changes in crystallite size of over  $\sim 10$  nm. Contrarily, aerobic oxidation should decrease the mean particle size and increase line broadening. This implies

that the narrowing is dominated by a decrease in crystallographic strain and is not largely influenced by changes in the mean particle size. We also attribute some line broadening of HPHT diffraction peaks to strain induced affects, but conclude they are qualitatively less than DND due to a lower surface-to-volume ratio and enhanced crystallographic structure (see TEM and Raman). Debye-Scherrer analysis would inherently show broader peaks due to the 5 nm crystallite size of DND, but the broadening is a convolution of both crystallite size, defects and strain.<sup>23</sup> In contrast, we find linewidths increase from  $\Delta 2\theta=1.362 \rightarrow 1.517$  after oxidation of

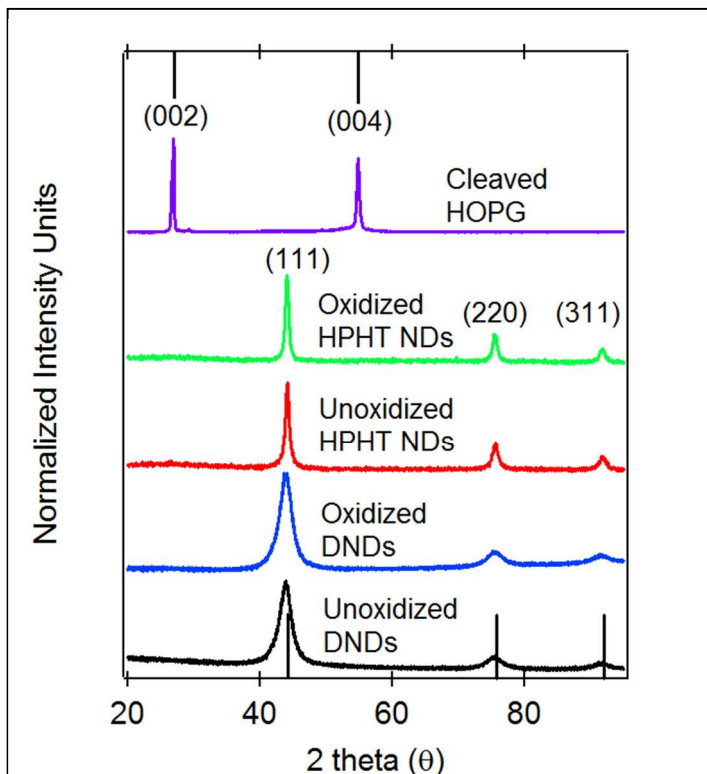


**Figure S5.** (A) XRD of a cleaved HOPG slab, unoxidized HPHT NDs, oxidized HPHT NDs (aerobic oxidation at  $575^{\circ}\text{C}$  for 2 hours) and oxidized DNDs, reveal the 002 and 004 reflections of graphite and the 111, 220 and 311 reflections of diamond, respectively. The broad signal from  $2\theta=20-40$  is from the  $\text{SiO}_2$  sample substrate. The 111 reflection for HPHT NDs and DNDs was observed at  $2\theta=44.14$  and  $2\theta=43.85$ . Standard diamond XRD patterns have a value of  $2\theta=44.14$ . No signature for crystalline graphite was observed in unoxidized and oxidized HPHT ND samples, consistent with Raman and TEM studies.

DND. Analysis of the DND diffraction pattern gives a grain size of 7.7 nm and 6.8 nm. This is ~1.8-2.7 nm larger than the 5 nm diameter commonly observed in DND and implies that additional contributions increase the line shape.<sup>23</sup> If strain were reduced we would expect line narrowing as well in the oxidized DND. The broadening implies that grain size was a more dominant factor in DND samples and strain was qualitatively constant. While an in-depth study of these diffraction patterns is beyond the scope of this paper, our conclusion that the HPHT NDs have superior crystallographic properties in comparison to DND is supported by both peak position and line width observations. We also observe no graphitic carbon before or after the oxidation of HPHT ND powders, and was consistent with the lack of D and G bands in visible-Raman scattering spectra. Graphite was only observed after high temperature vacuum annealing and is discussed below.

## Induced Graphitization After Vacuum Annealing at 900-1100°C

Raman signatures of graphitized HPHT after high temperature vacuum annealing are distinct from the  $sp^2$  derived modes observed after oxidative purification. Vacuum annealing of oxidized HPHT powders at 900-1100°C readily show D and G bands at  $1328\text{ cm}^{-1}$  and  $1572\text{ cm}^{-1}$ . Graphitization of HPHT NDs occurs  $200\text{ }^\circ\text{C}$  above DND graphitization and  $500\text{ }^\circ\text{C}$  below that of bulk diamond.<sup>24,25</sup>

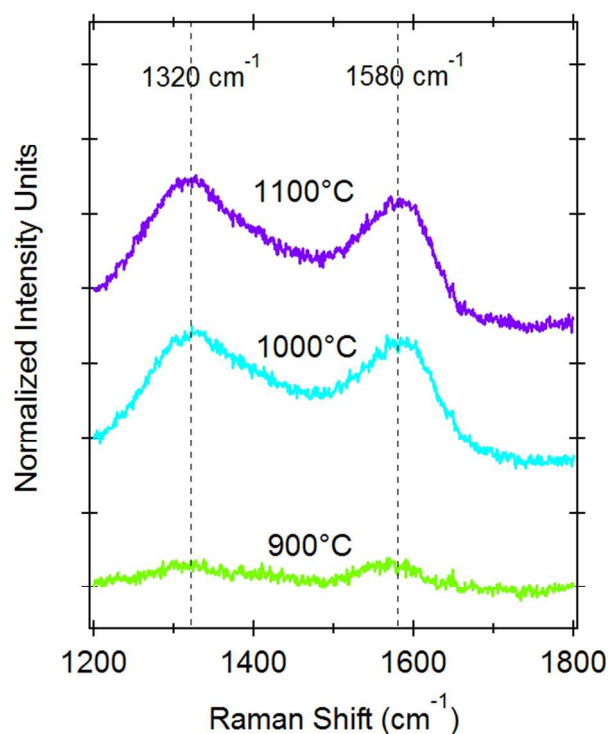


**Figure S6.** Visible Raman scattering ( $E_x=633\text{ nm}$ ) of high temperature vacuum annealing of HPHT ND powders readily shows D and G band phononic features. From 900-1100°C the reconstruction of the alcohol rich surface leads to a disordered graphite surface with peak positions at  $1328\text{ cm}^{-1}$  and  $1572\text{ cm}^{-1}$ . These features are distinct from those after oxidation from  $1280\text{-}1660\text{ cm}^{-1}$  which are attributed to Pandey reconstruction or ball milled derived sub-surface damage.

**Thermal Decomposition of HPHT Nanodiamonds.** Graphene nanoparticles were observed with HRTEM in samples that had been vacuum annealed at 750°C. These graphene nanoparticles were highly unstable under illumination with a 200 keV electron beam, in contrast to the high stability of diamond. The center of the graphene nanoparticle in Figure S4A is occupied with carbon atoms after electron irradiation (S4A→C).

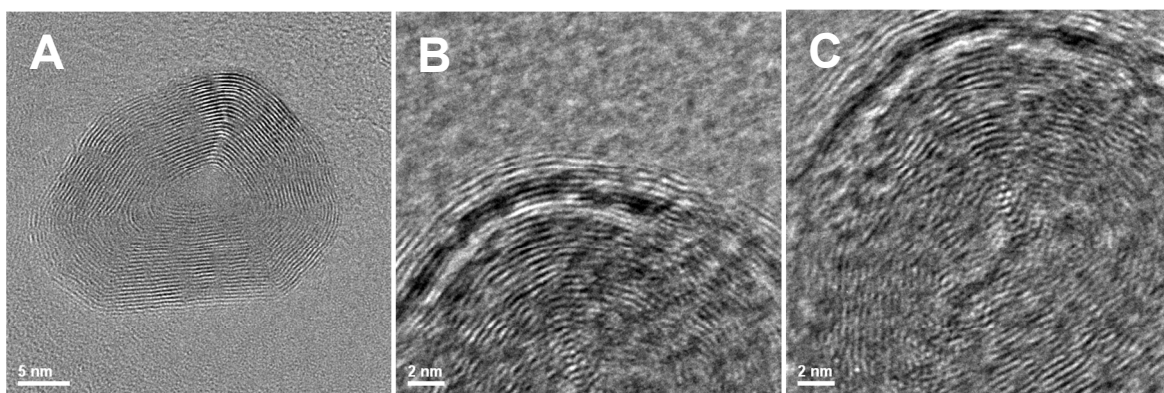


**Figure S7.** HREM images of an exfoliated HPHT ND that formed a “graphene onion”. The HPHT ND powder had been aerobically oxidized at 525°C to remove amorphous carbon, vacuum annealed at 700°C, and then reoxidized at 525°C. The interplanar spacing of the graphene layers was measured to be ~3.7 Å which is in agreement with previous studies on graphene onions.

**Oxidation of HPHT NDs with persulfuric acid followed by aerobic oxidation at 575°C.** 100 mg of unoxidized HPHT NDs were oxidized in a Piranha solution (30 mL  $\text{H}_2\text{SO}_4$  + 10 mL  $\text{H}_2\text{O}_2$ ) at 80°C for 24 hours. Vigorous bubbling was observed from the ND slurry for the first 25 minutes and then subsided. The resulting HPHT ND slurry was then diluted with 50 mL of 18 M $\Omega$   $\text{H}_2\text{O}$ , and centrifuged at 5000 rcf. The supernatant was discarded and the process repeated twice more. The powders were then oxidized in a tube furnace at 575°C for 2 hours in a ceramic boat and collected.

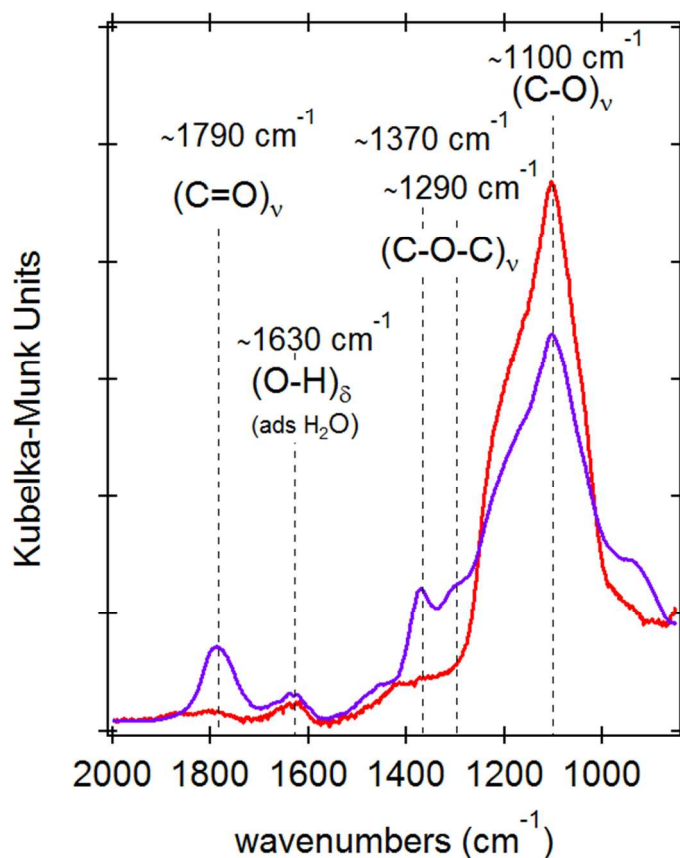


**Figure S8.** DRIFTS spectrum of HPHT NDs oxidized with persulfuric acid and then aerobically oxidized at 575°C. Vibrational modes for acid/acid anhydride groups  $(\text{C=O})_{\text{v}}$  are largely eliminated while alcohol/ether vibrations are unperturbed. In conjunction with the reduction of the carbonyl vibrational band from acids/acid anhydrides, there is a consummate reduction in the  $(\text{C-O-C})_{\text{v}}$  bridging mode as well.

## Quantitative Analysis of FT-IR Data.

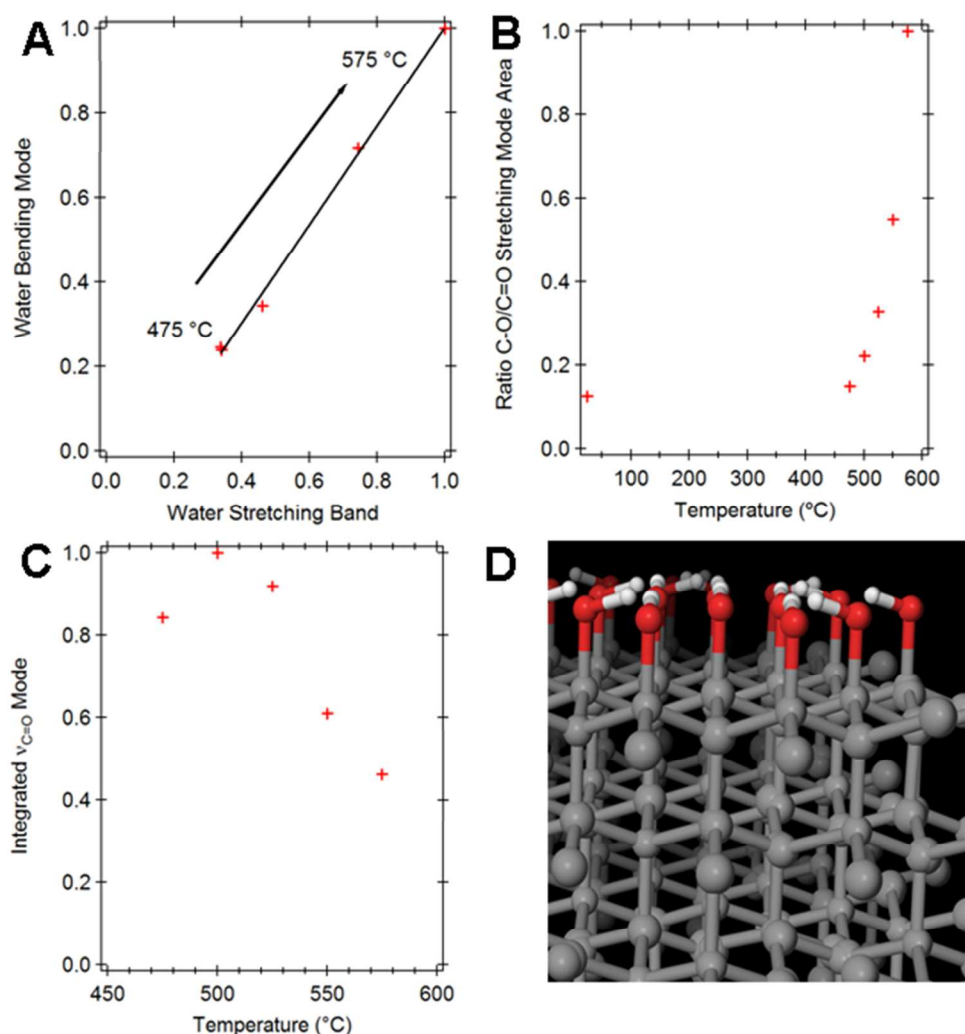


**Figure S9.** Integration of normalized DRIFTS spectra plotted to reveal trends in ratios of functional groups as a function of oxidation temperature. (A) The water stretching band ( $\nu_{O-H}$ ) was integrated and normalized to its maximum value and plotted versus the integrated peak for the bending mode of water ( $\delta_{O-H}$ ) at  $1630\text{ cm}^{-1}$  revealing a linear correlation and confirming its assignment. The steady increase in their intensities also reveals an increased hydrophilicity of the sample as the temperature of oxidation increases. (B) The ratio of integrated ( $\nu_{C-O}$ ):( $\nu_{C=O}$ ) stretching modes is plotted versus oxidation temperature and reveals that the relative carboxyl content decreases as oxidative temperatures increases. (C) Integrated  $\nu(C=O)$  mode normalized by ND concentration is shown versus oxidation temperature, and shows a maximum C=O component at a temperature of  $500^{\circ}\text{C}$ . (D) A cartoon depiction of an alcohol rich diamond (111) surface produced using Maestro.

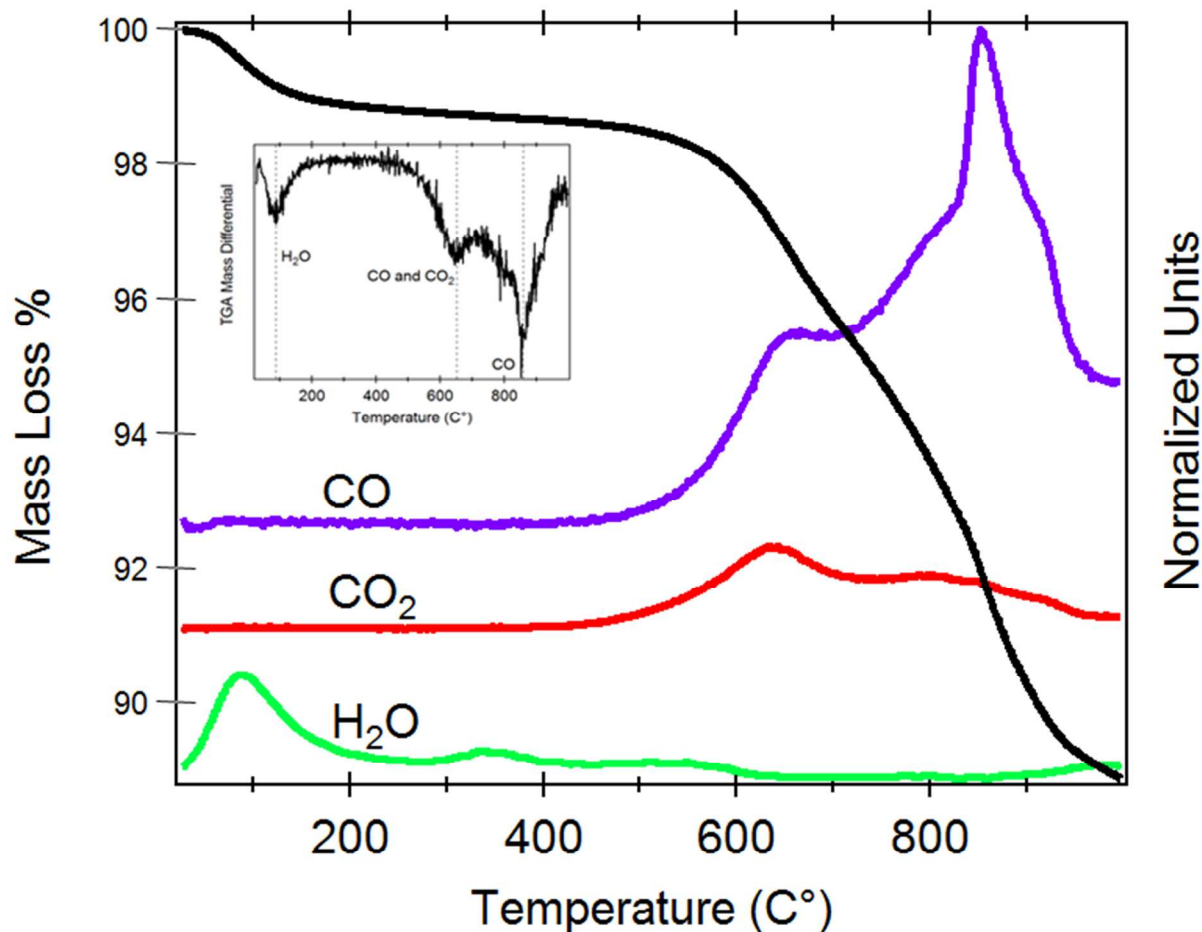


**Figure S10.** Anaerobic temperature programmed desorption mass spectrometry. Aerobically oxidized HPHT NDs were studied using temperature programmed desorption and mass spectrometry. Thermal desorption products were identified and plotted as function of temperature in Figure S10. The first species to desorb was H<sub>2</sub>O and it begins to desorb at temperatures above 30 °C and has three separate regimes of desorption as the sample is heated to 600 °C. It has been previously observed that oxygenated surface functional groups can desorb as H<sub>2</sub>O at temperatures as high as 600 °C or more.<sup>26,27</sup> CO<sub>2</sub> begins to desorb at 400 °C, peaks at 640 °C, and continues past 800 °C. The range of CO<sub>2</sub> desorption from 400 – 950 °C seen in Figure S10 is 100 °C higher in temperature than that found in diamond powders previously.<sup>28</sup> CO desorption was found to begin at 450 °C with a sharp features at 660 °C and 860 °C and a decline in signal until 1000 °C. The temperature range of CO desorption is similar that found in bulk diamond powder (500 °C), but lower than that observed for “clean” (111) single crystal diamond surfaces (790 °C and 1030 °C).<sup>29</sup> In another study hydroxyl terminated single crystal (111) surfaces were found to desorb CO at 648 °C.<sup>30</sup>

## Supporting References

- 1 Osswald, S., Yushin, G., Mochalin, V., Kucheyev, S. O. & Gogotsi, Y. Control of sp<sup>2</sup>/sp<sup>3</sup> Carbon Ratio and Surface Chemistry of Nanodiamond Powders by Selective Oxidation in Air. *J. Amer. Chem. Soc.*, **2006**, 128, 11635-11642.
- 2 Gago, R.; Jimenez, I.; Albella, J. M.; Climent-Font, A.; Caceres, D.; Vergara, I.; Banks, J. C.; Doyle, B. L.; Terminello, L. J. Bonding and Hardness in Nonhydrogenated Carbon Films with Moderate sp<sup>3</sup> Content. *J. App. Phys.* **2000**, 87, 8174-8180.
- 3 Kulik, J.; Lempert, G. D.; Grossman, E.; Marton, D.; Rabalais, J. W.; Lifshitz, Y. sp<sup>3</sup> Content of Mass-Selected Ion-Beam-Deposited Carbon Films Determined by Inelastic and Elastic Electron Scattering. *Phys. Rev. B.* **1995**, 52, 15812-15822.
- 4 Socrates, G. *Infrared and Raman Characteristic Group Frequencies: Tables and Charts*. 3rd edn, (John Wiley and Sons, **2001**).
- 5 Krueger, A., Stegk, J., Liang, Y., Lu, L. & Jarre, G. Biotinylated nanodiamond: Simple and Efficient Functionalization of Detonation Diamond. *Langmuir*, **2008**, 24, 4200-4204.
- 6 Krueger, A. & Lang, D. Functionality is Key: Recent Progress in the Surface Modification of Nanodiamond. *Adv. Funct. Mat.*, **2012**, 22, 890-906
- 7 Girard, H. A.; Petit, T.; Perruchas, S.; Gacoin, T.; Gessert, C.; Arnault, J.C. & Bergonzo, P. Surface Properties of Hydrogenated Nanodiamonds: a Chemical Investigation. *Phys. Chem. Chem. Phys.* **2011**, 13, 11517-11523.
- 8 Yeh, J. J. & Lindau, I. Atomic Subshell Photoionization Cross Sections and Asymmetry Parameters:  $1 \leq Z \leq 103$ . *Atomic Data and Nuclear Data Tables* **1985**, 32, 1-155.
- 9 Graupner, R., Maier, F., Ristein, J., Ley, L. & Jung, C. High-Resolution Surface-Sensitive C 1s Core-Level Spectra of Clean and Hydrogen-Terminated Diamond (100) and (111) Surfaces. *Phys. Rev. B* **1998**, 57, 12397-12409.
- 10 Makau, N. W. & Derry, T. E. Study of Oxygen on the Three Low Index Diamond Surfaces by XPS. *Surf. Rev. Lett.*, **2003**, 10, 295-301.
- 11 Loh, K. P.; Xie, X.N.; Lim, Y.H.; Teo, E.J.; Zheng, J.C. & Ando, T. Surface Oxygenation Studies on (100)-Oriented Diamond Using an Atom Beam Source and Local Anodic Oxidation. *Surf. Sci.* **2002**, 505, 93-114.
- 12 Stacey, A., Cowie, B. C. C., Orwa, J., Prawer, S. & Hoffman, A. Diamond C 1s Core-Level Excitons: Surface Sensitivity. *Phys. Rev. B* **2010**, 82, 125427 .
- 13 Noiset, O., Schneider, Y. J. & MarchandBrynaert, J. Surface Modification of Poly(aryl ether ether ketone) (PEEK) Film by Covalent Coupling of Amines and Amino Acids Through a Spacer Arm. *J. Poly. Sci. a-Poly. Chem.* **1997**, 35, 3779-3790.
- 14 Rutter, M. J. & Robertson, J. Ab Initio Calculation of Electron Affinities of Diamond Surfaces. *Phys. Rev. B* **1998**, 57, 9241-9245 .
- 15 Szunerits, S. & Boukherroub, R. Different Strategies for Functionalization of Diamond Surfaces. *J. Sol. Sta. Electro.* **2008**, 12, 1205-1218.
- 16 Jackson, S. T. & Nuzzo, R. G. Determining Hybridization Differences for Amorphous Carbon from the XPS C 1s Envelope. *Appl. Surf. Sci.* **1995**, 90, 195-203.
- 17 Wang, M.; Simon, N.; Charrier, G.; Bouttemy, M.; Etcheberry, A.; Li, M.S.; Boukherroub, R. & Szunerits, S. Distinction Between Surface Hydroxyl and Ether Groups on Boron-Doped Diamond Electrodes Using a Chemical Approach. *Electro. Comm.* **2010**, 12, 351-354.
- 18 Cui, J. B., Graupner, R., Ristein, J. & Ley, L. Electron Affinity and Band Bending of Single Crystal Diamond(111) Surface. *Diam. Rel. Mat.* **1999**, 8, 748-753.



- 19 Cui, J. B., Ristein, J. & Ley, L. Electron Affinity of the Bare and Hydrogen Covered Single Crystal Diamond (111) Surface. *Phys. Rev. Lett.* **1998**, 81, 429-432.
- 20 Petrini, D. & Larsson, K. Theoretical Study of the Thermodynamic and Kinetic Aspects of Terminated (111) Diamond Surfaces. *J. Phys. Chem. C* **2008**, 112, 3018-3026.
- 21 Staudacher, T.; Ziem, F.; Haussler, L.; Stohr, R.; Steinert, S.; Reinhard, F.; Scharpf, J.; Denischenko, A. & Wrachtrup, J. Enhancing the Spin Properties of Shallow Implanted Nitrogen Vacancy Centers in Diamond by Epitaxial Overgrowth. *Appl. Phys. Lett.* **2012**, 101, 212401.
- 22 Ofori-Okai, B. K.; Pezzagna, S.; Chang, K.; Loretz, M.; Schirhagl, R.; Tao, Y.; Moores, B.A.; Groot-Berning, K.; Meijer, J. & Degen, C.L. Spin Properties of Very Shallow Nitrogen Vacancy Defects in Diamond. *Phys. Rev. B* **2012**, 86, 081406.
- 23 Osswald, S., Havel, M., Mochalin, V., Yushin, G. & Gogotsi, Y. Increase of Nanodiamond Crystal Size by Selective Oxidation. *Diam. Rel. Mat.* **2008**, 17, 1122-1126.
- 24 Petit, T., Arnault, J. C., Girard, H. A., Sennour, M. & Bergonzo, P. Early Stages of Surface Graphitization on Nanodiamond Probed by X-Ray Photoelectron Spectroscopy. *Phys. Rev. B* **2011**, 23, 233407.
- 25 Seal, M. Graphitization of Diamond *Nature* **1960**, 185, 522-523
- 26 Laikhtman, A., Lafosse, A., Le Coat, Y., Azria, R. & Hoffman, A. Interaction of Water Vapor with Bare and Hydrogenated Diamond Film Surfaces. *Surf. Sci.* **2004**, 551, 99-105.
- 27 Ando, T., Ishii, M., Kamo, M. & Sato, Y. Thermal Hydrogenation of Diamond Surfaces Studied by Diffuse Reflectance Fourier-Transform Infrared, Temperature-Programmed Desorption and Laser Raman-Spectroscopy. *J. Chem. Soc.-Fara. Trans.* **1993**, 89, 1783-1789.
- 28 Ando, T., Ishii, M., Kamo, M. & Sato, Y. Thermal Hydrogenation of Diamond Surfaces Studied by Diffuse Reflectance Fourier-Transform Infrared, Temperature-Programmed Desorption and Laser Raman-Spectroscopy. *J. Chem. Soc.-Fara. Trans.* **1993**, 89, 1783-1789.
- 29 Bobrov, K., Schechter, H., Hoffman, A. & Folman, M. Molecular Oxygen Adsorption and Desorption from Single Crystal Diamond (111) and (110) surfaces. *Appl. Surf. Sci.*, **2002**, 196, 173-180.
- 30 Loh, K. P., Xie, X. N., Yang, S. W. & Zheng, J. C. Oxygen Adsorption on (111)-Oriented Diamond: A Study with Ultraviolet Photoelectron Spectroscopy, Temperature-Programmed Desorption, and Periodic Density Functional Theory. *J. Phys. Chem. B* **2002**, 106, 5230-5240.